

Diverse tsunamigenesis triggered by the Hunga Tonga-Hunga Ha'apai eruption

<https://doi.org/10.1038/s41586-022-05170-6>

Received: 25 February 2022

Accepted: 1 August 2022

Published online: 8 August 2022

 Check for updates

Patrick Lynett^{1✉}, Maile McCann¹, Zili Zhou¹, Willington Renteria¹, Jose Borrero^{1,2}, Dougal Greer², Ofa Fa'anunu³, Cyprien Bosserelle⁴, Bruce Jaffe⁵, SeanPaul La Selle⁵, Andrew Ritchie⁵, Alexander Snyder⁵, Brandon Nasr⁵, Jacqueline Bott⁶, Nicholas Graehl⁶, Costas Synolakis¹, Behzad Ebrahimi¹ & Gizem Ezgi Cinar¹

On the evening of 15 January 2022, the Hunga Tonga-Hunga Ha'apai volcano¹ unleashed a violent underwater eruption, blanketing the surrounding land masses in ash and debris^{2,3}. The eruption generated tsunamis observed around the world. An event of this type last occurred in 1883 during the eruption of Krakatau⁴, and thus we have the first observations of a tsunami from a large emergent volcanic eruption captured with modern instrumentation. Here we show that the explosive eruption generated waves through multiple mechanisms, including: (1) air–sea coupling with the initial and powerful shock wave radiating out from the explosion in the immediate vicinity of the eruption; (2) collapse of the water cavity created by the underwater explosion; and (3) air–sea coupling with the air–pressure pulse that circled the Earth several times, leading to a global tsunami. In the near field, tsunami impacts are strongly controlled by the water-cavity source whereas the far-field tsunami, which was unusually persistent, can be largely described by the air–pressure pulse mechanism. Catastrophic damage in some harbours in the far field was averted by just tens of centimetres, implying that a modest sea level rise combined with a future, similar event would lead to a step-function increase in impacts on infrastructure. Piecing together the complexity of this event has broad implications for coastal hazards in similar geophysical settings, suggesting a currently neglected source of global tsunamis.

The Kingdom of Tonga consists of hundreds of islands spanning 800 km from north to south. The archipelago lies along the Tonga–Kermadec Ridge, a submarine mountain range astride the most seismically active subduction boundary on Earth, thus sustaining a high rate of submarine volcanoes⁵. The Hunga Tonga-Hunga Ha'apai volcano (herein referred to as Hunga Tonga) is one of a number of active volcanoes in the area^{6,7} and began an active phase in late 2021. Owing to intermittent eruptions between 29 December 2021 and 4 January 2022, the emergent land area at Hunga Tonga increased from approximately 3 km² in early December to 5 km² in January, as pictured in Fig. 1a,b. After several days of decreased activity, the submarine volcano unleashed a series of intense, explosive eruptions starting near 04:15 UTC (17:15 local time) on 15 January 2022 (refs. ^{3,8}). Nearly 5 km² of land area vanished, leaving behind two small islands. Satellite photographs demonstrating these notable changes are shown in Fig. 1a,b. The eruption generated a global tsunami⁹, a phenomenon last observed nearly 140 years ago.

On 27 August 1883, the Krakatau volcano in the Sunda Strait between Java and Sumatra produced four explosive eruptions over 5 h generating a series of tsunami waves, causing the destruction of hundreds of towns and villages and killing at least 36,000 people^{4,10,11}. Sea level disturbances observed in the far field were due to coupling of the sea

surface and air–pressure pulses generated from the great explosion of Krakatau¹². The tsunami was recorded by notably distant tidal gauges, such as that at the Gulf of Aden 11,000 km away from the source¹³.

The complex and globally observed tsunamis generated by Krakatau in 1883 are analogous to those caused by Hunga Tonga, because the former's explosive eruption generated tsunamis recorded throughout the world's oceans. In this paper, through analysis of instrumental data, satellite imagery, post-event surveys and detailed hindcast modelling, we show that, similar to the 1883 Krakatau event, the Hunga Tonga eruption generated tsunamis through different mechanisms occurring at distinct times. We also discuss global observations and impacts of this event, the source mechanisms of the tsunami waves and our efforts to resolve the mechanics of generation through numerical modelling.

Tsunami observations and impacts

We first examined eye-witness accounts and observed impacts from the tsunami, starting from locations nearest to the source. Owing to travel restrictions in Tonga associated with the COVID-19 pandemic, no comprehensive surveys of tsunami run-up or inundation extents were completed although such efforts are presently under way. Therefore,

¹Tsunami Research Center, Sonny Astani Department of Civil and Environmental Engineering, University of Southern California, Los Angeles, CA, USA. ²eCoast Marine Consulting and Research, Raglan, New Zealand. ³Tonga Meteorological Service, Nuka'alofa, Tonga. ⁴New Zealand National Institute of Water and Atmosphere, Christchurch, New Zealand. ⁵United States Geological Survey, Pacific Coastal and Marine Science Center, Santa Cruz, CA, USA. ⁶California Geological Survey, Sacramento, CA, USA. [✉]e-mail: plynett@usc.edu

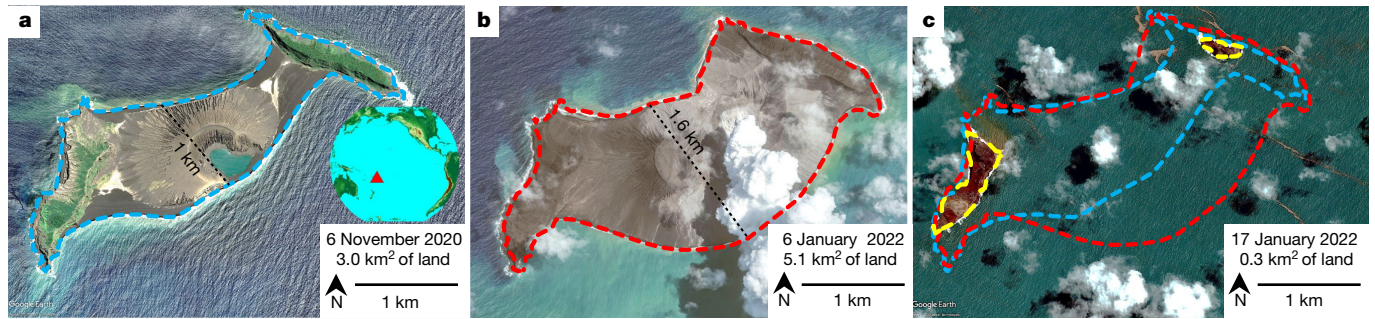


Fig. 1 | Changes in land area of Hunga Tonga before and after the eruption.

a–c, Satellite imagery from before the recent active phase on 6 November 2020 (a), during the active phase but before the eruption on 6 January 2022 (b) and on 17 January 2022 after the eruption (c). Shoreline boundaries are denoted by blue (a), red (b) and yellow (c) dashed lines. The location of the Hunga Tonga

volcano is represented by the red triangle on the globe inset in a. Original satellite imagery was sourced from Google Earth/Maxar Technologies (a,c) and from Getty/Maxar Technologies (b), with similar imagery provided by UNOSAT⁴¹; global bathymetry data were sourced from GEBCO⁴². Land area was calculated from the imagery, using edge detection to determine land borders⁴³.

we rely on eye-witness accounts and scant quantitative data provided by local investigators. For example, a weather station positioned on a mobile phone tower with base at a ground elevation of approximately 13 m above sea level was destroyed by the tsunami in Kanokupolu, a town in western Tongatapu. This station observed the onset of the eruption and reported data until 05:00 UTC (18:00 local time). Three days after the tsunami, a site visit showed that the tower had been toppled and transported approximately 20 m from its original location, suggesting tsunami flow elevations significantly more than 13 m above mean sea level.

Photographs and videos taken at a beach resort in Ha'atafu, also in western Tongatapu, demonstrate the scale of the destruction in the near field. The resort, situated at an estimated elevation of 5–10 m above mean sea level, was demolished. Built structures were reduced to their foundations and the original densely vegetated coastal forest was stripped to bare earth (Fig. 2). Eye-witness accounts from Ha'atafu indicate that an early wave arrived roughly 10 min before the primary tsunami and before the residents heard the largest explosions from the erupting volcano. The precursor wave is substantiated by a small signal on the Tongatapu tide gauge, which arrived too early, based on well-established tsunami celerity models¹⁴, to be a product of an eruption at 04:15 UTC. This smaller tsunami fortuitously acted as a warning and prompted initial evacuations in Tongatapu, probably averting loss of life. At the Tongan capital of Nuku'alofa, located on the more protected northern coast of Tongatapu, much lower tsunami flow elevations of less than 5 m above mean sea level were observed.

New Zealand's array of deep-ocean assessment and reporting of tsunamis (DART) tsunameters¹⁵ recorded tsunamis along the Tonga–Kermadec trench and to the west in the Coral Sea. From the initial wave, the sensors recorded peak-to-trough (P2T) heights of approximately 35 cm and wave periods of 10–40 min. Approximately 90 min later, the highest positive amplitude of just over 20 cm was recorded during a burst of relatively short (3–5 min) waves (see Methods for spectral analysis).

Coastal tide gauges around New Zealand, primarily in harbours, also clearly recorded the tsunami. However, the signal at some stations was complicated by the presence of storm waves due to post-tropical cyclone Cody, which was simultaneously affecting the region. Measured tsunami amplitudes ranged from 20 to 80 cm, with a peak positive amplitude of 1.3 m measured at Great Barrier Island off Auckland's east coast. The small marina at Tutukaka on the north-east coast of New Zealand is a well-known tsunami 'hotspot'¹⁶ and incurred severe damage during this event. Strong tsunami-induced currents entered and exited the marina through a narrow entrance between two breakwaters, causing damage to floating docks, tearing vessels from their moorings and leading to numerous collisions. Around New Zealand, bays and harbours prone to long-wave resonance were activated by the

surges, with Wellington harbour in particular showing a long-lasting resonant signal at its fundamental modes^{17,18} (Extended Data Fig. 1).

In the far field, tsunami impacts were observed and recorded by the authors at Ventura harbour, United States during the day on 15 January 2022. The leading crest of the air-pressure pulse arrived in Ventura at 11:54 UTC (03:54 local time), or 7.65 h after the explosion, and shortly thereafter initial oscillations in the harbour were detected. Larger waves started to arrive near 15:30 UTC (07:30 local time), with the peak intensity of the waves and associated damage observed in the late morning to afternoon on 15 January. Throughout the next 30 h, the tide gauge in the inner harbour recorded continuous tsunami amplitudes of at least ± 0.6 m, with the largest P2T heights of 1.8–2.4 m.

Observations of currents exiting Ventura harbour show that their speed increased as the tide receded, peaking at 21:00–23:00 UTC (13:00–15:00 local time), corresponding to lower tidal elevations. Most of the damage to fixed infrastructure occurred at low tide (22:51 UTC), or 11 h after the initial waves reached the harbour. Strong and swirling currents¹⁹ destroyed three major docks, including a 27 m section of dock attached to four pilings, a commercial dock holding multiple slips and a 9 m residential dock. Additionally, a total of 23 residential floating dock ramps were lifted from supports and carried out by the currents.

Farther north, in Santa Cruz harbour, USA, waves were first observed at 15:00 UTC (07:00 local time). The seventh tsunami crest after this time was the largest, arriving near high tide at 16:50 UTC (08:50 local time). This surge flooded parking lots and damaged vehicles, docks, bathrooms, dredging equipment and other infrastructure around the harbour. This damage was mainly the result of flooding of on-land facilities, which differs from the in-water infrastructure impacts experienced in Ventura harbour. However, during the highest-elevation tsunami crest, floating docks in the rear of Santa Cruz harbour were less than 30 cm from the tops of the piles, implying that a similar event at a slightly higher tide or sea level would have led to widespread destruction in the harbour. Maximum tsunami run-up at the harbour and nearby beaches was estimated by well-preserved wrack lines of plant material and driftwood, measured with survey-grade global positioning system receivers. At Santa Cruz harbour the highest run-up was 3.97 m above mean lower low water (MLLW), or 2.22 m above the predicted high tide²⁰. At beaches along Monterey Bay 10 and 13 km south-east of Santa Cruz harbour, tsunami run-up markers were surveyed at 3.71 and 4.28 m above MLLW.

In South America, widespread tsunami amplitudes of approximately 1 m were observed. Some coastal locations (Puerto Ayora, Ecuador; Callao, Peru; Arica, Chile; Coquimbo, Chile) experienced persistent sea level perturbations for more than 24 h. According to Peru's National Institute of Civil Defense, two people died because of the tsunami at Naylamp beach in Lambayeque District²¹. At Callao the first tsunami crest, probably generated by the air-pressure pulse, arrived around

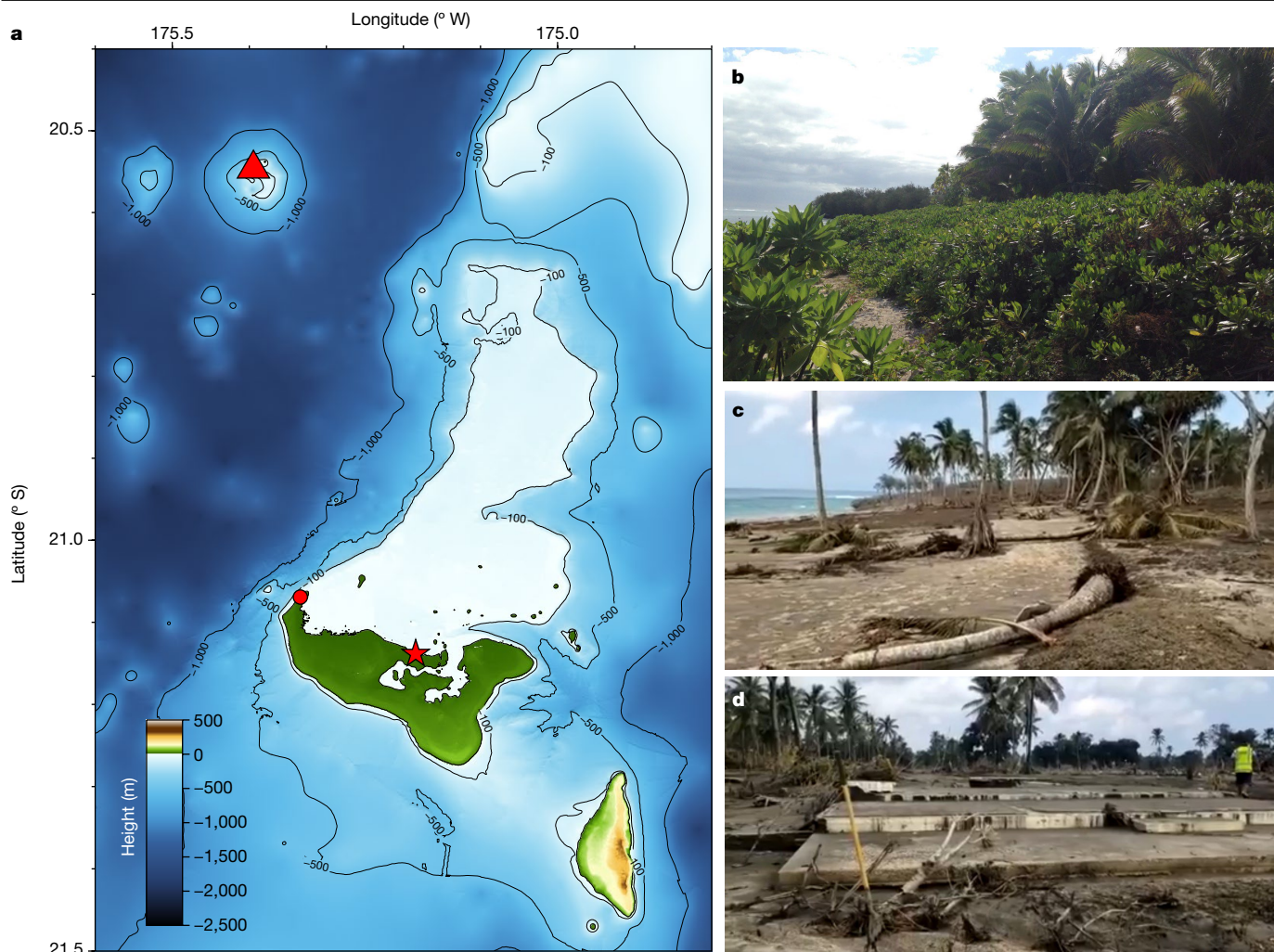


Fig. 2 | Tsunami impacts on the island of Tongatapu, Tonga. **a**, Locations of the volcano (red triangle), the main islands of Tongatapu and 'Eua to the south, photographs taken in the town of Ha'atafu (red circle), and the Nuku'alofa tide gauge (red star) overlaid on the seafloor elevation map. **b**, Photograph of the Ha'atafu area before the tsunami, showing the lush vegetation typical of this area. **c,d**, Images from Ha'atafu after the tsunami showing a beachfront

14:30 UTC (09:30 local time); the main, hazardous waves arrived 5 h later. In the nearby La Pampilla oil terminal the oil tanker vessel *Mare Doricum* reported the breaking of mooring ropes, which led to an oil release of approximately 6,000 barrels. By international standards, this is classified as a large oil spill²².

Pressure observations

In explosive eruptions of large volcanoes such as the Hunga Tonga event, tsunami generation occurs through two air–sea coupling stages²³. The first stage is immediately after the initial explosive eruption, when a high Mach number shock wave radiates away from the volcano. For an eruption energy in the range of 4–18 megatons of TNT (1.6×10^{16} – 7.5×10^{16} J), the shock wave would have travelled 2.9–4.8 km from the source before transitioning from a supersonic shock to a sonic wave, with initial Mach number greater than 6.0 and peak explosive pressure of more than 3,000 kPa (ref. ²⁴). Thus, for the Hunga Tonga eruption, the transition from shock wave to sonic wave would have occurred in just a few seconds following the eruption. The sonic wave continued its propagation away from the volcano at the speed of sound, reaching Tongatapu just over 3 min after the eruption.

stripped of vegetation (**c**) and the foundations of a washed-away structure (**d**). Map data are a blend of GEBCO⁴², nautical charts, light detection and ranging (LiDAR) topography, multi-beam bathymetry data, offshore surveys and hand-digitized data, as described in the Methods and plotted in Generic Mapping Tools. The photograph in **b** was taken by the authors, and those in **c,d** were provided to the authors by local residents.

Through a complex process driven by explosion and shock-wave-generated pressure, temperature and density gradients, a stable Lamb wave^{25,26} (herein stated as the air-pressure pulse) radiates out from the source through the lower atmosphere^{27,28}. This wave forms into a leading positive-pressure crest and a trailing negative-pressure trough, known as an N-wave²⁹. The moving pressure adds momentum to the ocean surface through a pressure-gradient forcing that pushes the ocean surface in the direction of the positive-pressure gradient³⁰. Following the Hunga Tonga eruption, the pressure pulse was captured on weather station pressure sensors around the world³¹ and was responsible for generating the far-field tsunami observed throughout the Pacific.

We developed an N-wave model for the evolution of the air-pressure pulse to recreate this tsunami generation mechanism. We calibrated this model using observational data from 143 weather stations throughout the Pacific, as summarized in Fig. 3 and discussed in detail in the Methods. The model accurately captures the arrival time, amplitude and shape of the air-pressure pulse, from the nearest pressure observation in Tongatapu to far-field locations in Japan and the United States. We emphasize that this model predicts the air-pressure pulse and not the early-time shock wave.

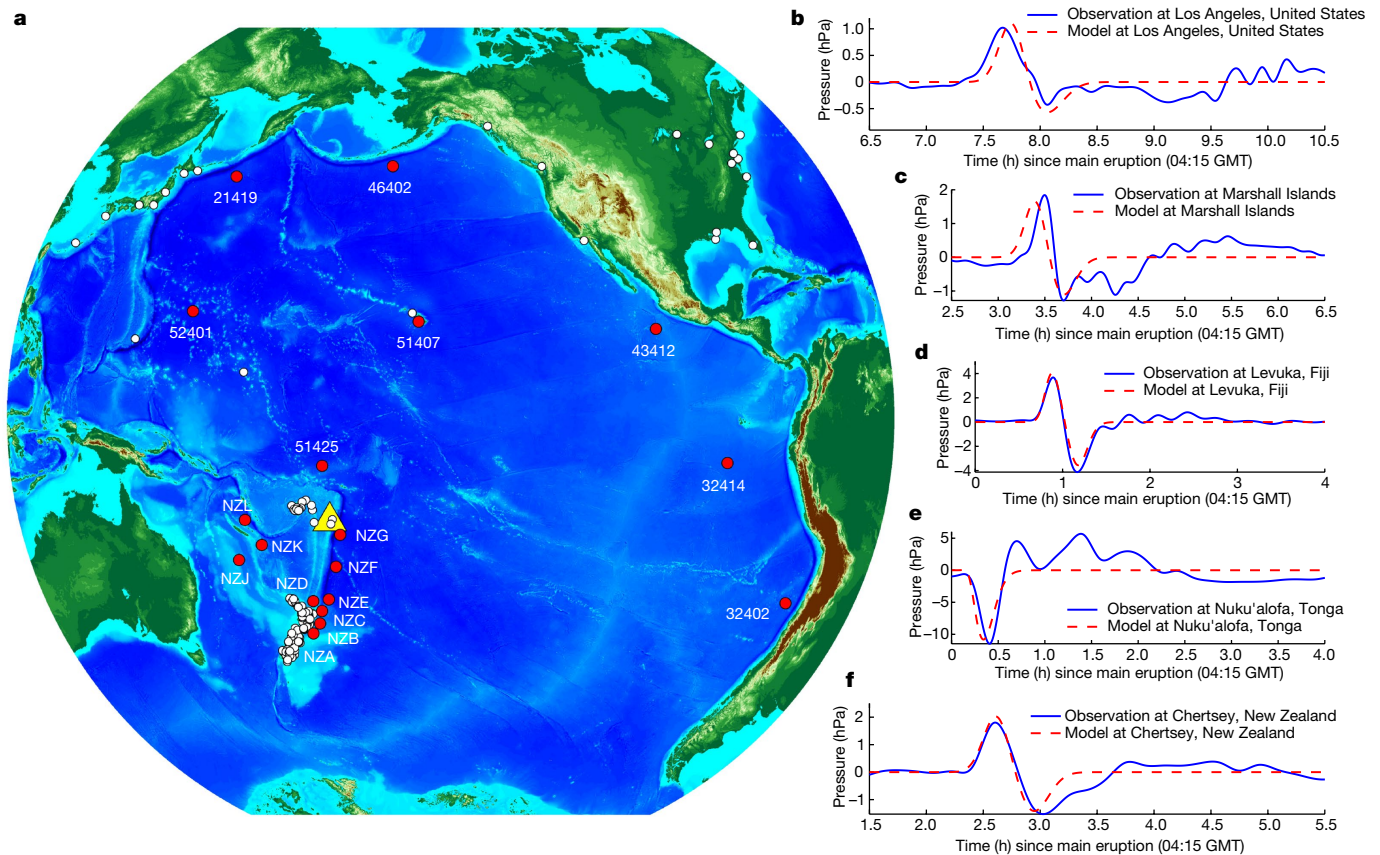


Fig. 3 | Meteorological and oceanographic data locations, and model–data pressure comparisons. **a**, Geographic locations of the 143 weather stations used to calibrate the pressure pulse model (white dots), the deep-sea DART sensors used to validate the tsunami model (red dots, with name labels) and the Hunga Tonga volcano (yellow triangle). **b–f**, Observed (blue line) and modelled (red dashed line) pressure pulse signals (in hPa; 1 hPa = 1 mb) for Los Angeles (b), Kwajalein, Marshall Islands (c), Levuka, Fiji (d), Nuku'alofa, Tonga (e) and

Chertsey, New Zealand (f). Additional model–data pressure comparisons are given in Extended Data Fig. 4. Pressure data provided by the National Oceanic and Atmospheric Association (NOAA), the Japan Meteorological Agency, the Fiji Meteorological Service and the Tonga Meteorological Service. Global bathymetry data were sourced from GEBCO⁴², and the map was plotted in MATLAB.

Tsunami modelling and discussion

Tsunamis were generated through three different mechanisms related to the explosive eruption near 04:15 UTC: (1) air–sea coupling with the early-time shock wave, (2) waves generated by the equilibrium response to the water cavity generated by the explosion and (3) air–sea coupling with the global air-pressure pulse. During volcanic eruptions, tsunamis may also be generated by submarine landslides, flank collapse, caldera collapse, pyroclastic density flows or submarine jets^{23,32,33}; our focus here is on waves generated by the large initial explosion. We performed the tsunami simulation using a highly nonlinear dispersive water wave code³⁴, as described in Methods. We remark here that, because of the widespread and energetic 3–5-min period when waves were observed in the DART tsunami data (Extended Data Fig. 1), the use of a dispersive model is necessary to properly capture water wave propagation. Figure 4 summarizes the simulation results, and additional comparisons are provided in Methods.

The water level observation most challenging to explain is the measurement nearest to the source—the tide gauge at Nuku'alofa, Tonga, approximately 65 km from the volcano. The shock wave and cavity source in our model can recreate the tide signal starting at 0.4 h (around 25 min) after the eruption. It is physically impossible for a water wave to arrive at the tide station earlier than this time if generated by the explosive eruption at 04:15 UTC. However, the tide station data at Nuku'alofa shows a series of relatively small-amplitude waves arriving just 10 min after the eruption. These early waves would have arrived on the western-facing beaches of north-west Tongatapu immediately before or during the 04:15

UTC eruption and three or more minutes before residents would have heard the explosion, which is consistent with eye-witness accounts at this location. Thus, we can confidently state that there was a small tsunami source before the main eruption. Whereas the available water level data for this precursor tsunami are too limited for precise description of the source, it is plausible that the tsunami was generated by an earlier minor eruption and/or a submarine mass movement occurring between 04:00 and 04:05 UTC which, in turn, may have destabilized the caldera and led to the explosive eruption 10 min later.

Further from the volcano, the tsunami generated by the air-pressure pulse is significant in the DART data. Whereas the physics of tsunami-generis by a moving pressure pulse are well understood^{35,36}, the wave field nonetheless becomes highly complex. Using weather station observations and satellite imagery (Methods and Extended Data Fig. 2), we calculate the speed of the pressure crest, or the celerity, to be $311 \pm 20 \text{ m s}^{-1}$ at locations in the far field, with variability in this speed depending on direction of propagation but in agreement with theory³⁵. At this speed, the air-pressure pulse moves faster than the tsunami in all depths less than 9.9 km. At a depth of 9.9 km the speed of the pressure pulse and that of the tsunami match, a phenomenon known as Proudman resonance³⁷ occurs and the amplitude of the tsunami grows rapidly. Whereas a speed match represents the optimal conditions for maximization of tsunami height, the amplitude of the tsunami generated by the air-pressure pulse will increase as speed match is approached³⁸. For example, the air-pressure pulse creates a tsunami of greater height in 5 km of water than in 1 km, even though

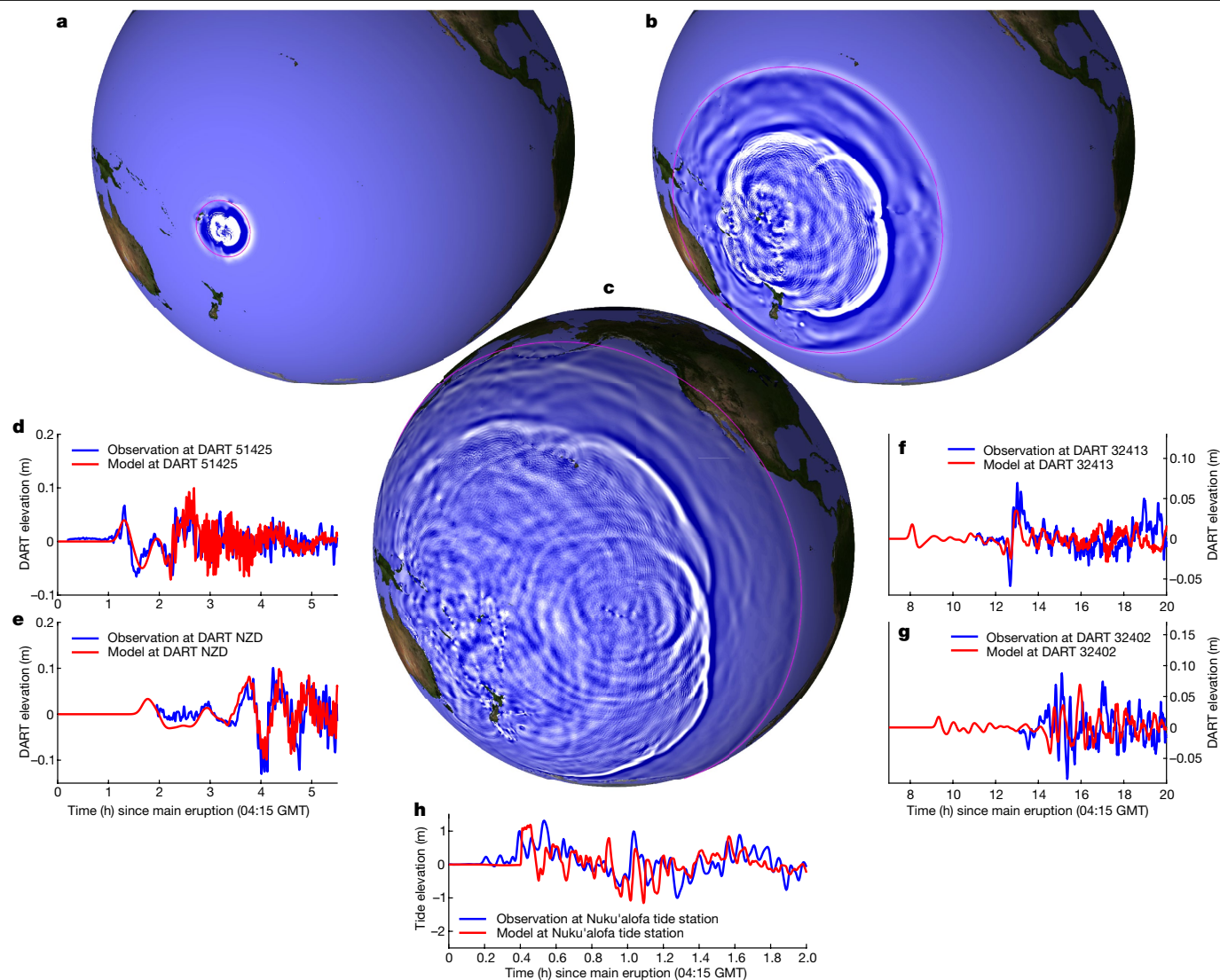


Fig. 4 | Tsunami evolution throughout the Pacific Ocean. **a–c**, Summary of simulation results from the highly nonlinear dispersive water wave model we used to recreate the tsunamis generated by this event. The wave field in the Pacific is shown at three different times on the globes at 1 h post eruption (05:15 UTC) (**a**), 4 h post eruption (08:15 UTC) (**b**) and 8 h post eruption (12:15 UTC) (**c**). In each of these plots, the crest location of the pressure pulse is given by the magenta line; note how in **c** the pressure pulse, crossing into North America, has far outrun the main tsunami it generated earlier, which at this time has just

Proudman resonance is never reached. This effect was clearly observed during the Hunga Tonga eruption. As the air-pressure pulse passed over the Tonga–Kermadec Trench, with widespread water depths of more than 9 km, the amplitude of the tsunami rapidly increased sending an energetic beam of energy towards the Americas. The air-pressure pulse then outran the tsunami it generated over the trench, leaving behind a slower-moving ‘free’ gravity-wave tsunami and continuing to generate small wave disturbances while passing over irregular bathymetry.

In the South Pacific, as observed by DART stations NZD, NZG and 51425 (Fig. 4), the tsunami signal is composed of (1) the ‘pressure-forced’ tsunami carried by the air-pressure pulse arriving first, (2) the free tsunami generated by the air-pressure pulse earlier in the event with periods of 10–25 min and (3) short waves generated by the cavity collapse and/or possibly other complex sources at the volcano, with periods of 3–5 min. Tsunami types 2 and 3 arrive tens of minutes to hours after that of 1. We note that, for the tsunami associated with 1, the DART sensor, which is an ocean bottom pressure recorder, measures both pressure from the amplitude of the tsunami

passed through Hawaii. **d–h**, Model–data comparisons are given in the time series plots at DART stations 51425 (**d**), NZD (**e**), 32413 (**f**) and 32402 (**g**) (locations given in Fig. 3), as well as at the Nuku’alofo tide station (**h**; location given in Fig. 2). In the DART comparisons, the red line represents modelled ocean surface elevation including the pressure head from the pressure pulse, and the blue line represents the observed data. Additional model–data tsunami comparisons are given in Extended Data Figs. 5 and 6, and data sources are described in the Methods. Globe map plotted in MATLAB.

and the air pressure acting on it. This implies that, during these events, the type of water level sensor (that is, bottom pressure sensor versus surface float or surface radar) will yield different estimates of water level, because some will capture the air pressure and some will not.

In Hawaii (and DART station 51407) the air-pressure pulse arrived approximately 4.5 h after the eruption, followed by the main tsunami, composed primarily of waves generated earlier by the pressure pulse when passing through the Central Pacific Basin, at 7 h after the eruption. In the East Pacific, the passing of the air-pressure pulse did not trigger the DART system to enter its high-frequency sampling mode at stations 32413 and 32402. This mode did not activate until the larger free tsunami, created as the pressure pulse passed over the Kermadec Trench, arrived 3–4 h later. A similar situation is found along the west coast of North America, where minor waves from the passage of the pressure pulse were predicted and observed around 12:00 UTC, with larger waves arriving hours later at 15:00 UTC. As the air-pressure pulse passed over the deep-water subduction zone trenches of the Pacific Ocean, the

Proudman resonance effect was activated, inducing a phenomenon where every major trench in the Pacific Basin effectively generated a small tsunami, with crest length equal to that of the trench. The result was tsunami energy generated from the entire extent of the Pacific Rim over the course of 12 h, leaving the Pacific Ocean filled with tsunamis travelling in all directions and causing the unique persistence of this event observed along coastlines and harbours throughout the Pacific.

In summary, we have demonstrated that the explosive eruption of the Hunga Tonga volcano generated tsunamis through different mechanisms, at different times and across a wide range of scales. Tsunami damage in the near field was severe, whereas far-field impacts were similar to those experienced during recent great earthquakes^{17,39,40}. Presently, tsunami hazard studies used for emergency planning, mitigation efforts and infrastructure design do not commonly consider volcanic source tsunamis. Understanding the Hunga Tonga event has broad implications for these studies, particularly for maritime and near-shoreline infrastructure under threat of sea level rise, where global tsunamis from large volcanic eruptions are currently neglected.

Online content

Any methods, additional references, Nature Research reporting summaries, source data, extended data, supplementary information, acknowledgements, peer review information; details of author contributions and competing interests; and statements of data and code availability are available at <https://doi.org/10.1038/s41586-022-05170-6>.

- Cronin, S. J. et al. New volcanic island unveils explosive past. *Eos* <https://doi.org/10.1029/2017EO076589> (2017).
- Witze, A. Why the Tongan eruption will go down in the history of volcanology. *Nature* **602**, 376–378 (2022).
- M 5.8 Volcanic Eruption – 68 km NNW of Nuku'alofa, Tonga, 15 January 2022 (USGS, retrieved 15 January 2022); <https://earthquake.usgs.gov/earthquakes/eventpage/us7000gc8r/executive>
- Self, S. & Rampino, M. R. The 1883 eruption of Krakatau. *Nature* **294**, 699–704 (1981).
- Schofield, J. C. Notes on the geology of the Tongan Islands. *N. Z. J. Geol. Geophys.* **10**, 1424–1428 (1967).
- Garvin, J. B. et al. Monitoring and modeling the rapid evolution of earth's newest volcanic island: Hunga Tonga Hunga Ha'apai (Tonga) using high spatial resolution satellite observations. *Geophys. Res. Lett.* **45**, 3445–3452 (2018).
- Brenna, M. et al. Post-caldera volcanism reveals shallow priming of an intra-ocean arc andesitic caldera: Hunga volcano, Tonga, SW Pacific. *Lithos* **412**, 106614 (2022).
- Poli, P. & Shapiro, N. M. Rapid characterization of large volcanic eruptions: measuring the impulse of the Hunga Tonga Ha'apai explosion from teleseismic waves. *Geophys. Res. Lett.* **49**, e2022GL098123 (2022).
- Carvajal, M., Sepúlveda, I., Gubler, A., & Garreaud, R. Worldwide signature of the 2022 Tonga volcanic tsunami. *Geophys. Res. Lett.* **49**, 6 (2022).
- Sigurdsson, H., Houghton, B., McNutt, S., Rymer, H. & Stix, J. *The Encyclopedia of Volcanoes* (Elsevier, 2015).
- Nomanbhoy, N. & Satake, K. Generation mechanism of tsunamis from the 1883 Krakatau eruption. *Geophys. Res. Lett.* **22**, 509–512 (1995).
- Pararas-Carayannis, G. Near and far-field effects of tsunamis generated by the paroxysmal eruptions, explosions, caldera collapses and massive slope failures of the Krakatau volcano in Indonesia on August 26–27, 1883. *Sci. Tsunami Hazards* **4**, 191–201 (2003).
- Jordan, B. R. Tsunamis of the Arabian Peninsula a guide of historic events. *Sci. Tsunami Hazards* **27**, 31 (2008).
- Yeh, H., Liu, P., Briggs, M. & Synolakis, C. Propagation and amplification of tsunamis at coastal boundaries. *Nature* **372**, 353–355 (1994).
- Fry, B. et al. Sensor network warns of stealth tsunamis. *Eos* <https://doi.org/10.1029/2020EO144274> (2020).
- Borrero, J. C., Goring, D. G., Greer, S. D. & Power, W. L. Far-field tsunami hazard in New Zealand ports. *Pure Appl. Geophys.* **172**, 731–756 (2015).
- Borrero, J. & Greer, S. D. Comparison of the 2010 Chile and 2010 Japan tsunamis in the far-field. *Pure Appl. Geophys.* **170**, 1249–1274 (2013).
- Gilmour, A. E. Response of Wellington harbour to the tsunamis of 1960 and 1964. *N. Z. J. Mar. Freshw. Res.* **24**, 229–231 (1990).
- Kalligeris, N. et al. Lagrangian flow measurements and observations of the 2015 Chilean tsunami in Ventura, CA. *Geophys. Res. Lett.* **43**, 5217–5224 (2016).
- La Selle, M. et al. *Observations of Tsunami and Runup Heights in Santa Cruz Harbor and Surrounding Beaches from the 2022 Hunga Tonga-Hunga Ha'apai Tsunami Technical Report* (USGS, 2022); <https://doi.org/10.5066/P9ZVAB8D>
- Inician acciones de respuesta luego de oleajes en el litoral (INDECI, 2022); <https://www.gob.pe/institucion/indeci/noticias/576687-inician-acciones-de-respuesta-luego-de-oleajes-en-el-litoral>
- Peru: Oil Spill, flash update no. 02 (UNOCHA, 2022); <https://reliefweb.int/report/peru/peru-oil-spill-flash-update-no-02-27-january-2022>
- Paris, R. Source mechanisms of volcanic tsunamis. *Philos. Trans. A Math. Phys. Eng. Sci.* **373**, 20140380 (2015).
- Medici, E. F., Allen, J. S. & Waite, G. P. Modeling shock waves generated by explosive volcanic eruptions. *Geophys. Res. Lett.* **41**, 414–421 (2014).
- Lamb, H. On the vibrations of an elastic sphere. *Proc. Lond. Math. Soc.* **1**, 189–212 (1881).
- Lamb, H. *Hydrodynamics* (Cambridge Univ. Press, 1932).
- Yokoo, A., Ichihara, M., Goto, A. & Taniguchi, H. Atmospheric pressure waves in the field of volcanology. *Shock Waves* **15**, 295–300 (2006).
- Garrett, C. J. R. Atmospheric edge waves. *Q. J. R. Meteorol. Soc.* **95**, 731–753 (1969).
- Fitzgerald, T. J. Observations of total electron content perturbations on GPS signals caused by a ground level explosion. *J. Atmos. Sol. Terr. Phys.* **59**, 829–834 (1997).
- Stoker, J. J. *Water Waves. The Mathematical Theory with Applications* (Interscience Publ. Inc., 1957).
- Amores, A. et al. Numerical simulation of atmospheric Lamb waves generated by the 2022 Hunga-Tonga volcanic eruption. *Geophys. Res. Lett.* <https://doi.org/10.1029/2022GL098240> (2022).
- Latter, J. H. Tsunamis of volcanic origin: summary of causes, with particular reference to Krakatoa, 1883. *Bull. Volcanol.* **44**, 467–490 (1981).
- Shen, Y. et al. Laboratory experiments on tsunamigenic discrete subaqueous volcanic eruptions. Part 2: properties of generated waves. *J. Geophys. Res. Oceans* **126**, e2020JC016587 (2021).
- Kim, D. H., Lynett, P. J. & Socolofsky, S. A. A depth-integrated model for weakly dispersive, turbulent, and rotational fluid flows. *Ocean Model. (Oxf.)* **27**, 198–214 (2009).
- Harkrider, D., Press, K. The Krakatoa air-sea waves: an example of pulse propagation in coupled systems. *Geophys. J. Int.* **13**, 149–159 (1967).
- Monserrat, S., Vilibić, I. & Rabinovich, A. B. Meteotsunamis: atmospherically induced destructive ocean waves in the tsunami frequency band. *Nat. Hazards Earth Syst. Sci.* **6**, 1035–1051 (2006).
- Proudman, J. The effects on the sea of changes in atmospheric pressure. *Geophys. J. Int.* <https://doi.org/10.1111/j.1365-246X.1929.tb05408.x> (1929).
- Vilibić, I. Numerical simulations of the Proudman resonance. *Cont. Shelf Res.* **28**, 574–581 (2008).
- Wilson, R. I. et al. Observations and impacts from the 2010 Chilean and 2011 Japanese tsunamis in California (USA). *Pure Appl. Geophys.* **170**, 1127–1147 (2013).
- Borrero, J. et al. Observations, effects and real time assessment of the March 11, 2011 Tohoku-oki tsunami in New Zealand. *Pure Appl. Geophys.* **170**, 1229–1248 (2013).
- UNOSAT Emergency Mapping service Activated over Tonga for the Volcanic Eruption and Induced Tsunami (UNITAR, accessed 20 January 2022); <https://unitar.org/about/news-stories/news/unosat-emergency-mapping-service-activated-over-tonga-volcanic-eruption-and-induced-tsunami>
- Gridded Bathymetry Data: GEBCO_2020 Grid (General Bathymetric Chart of the Oceans, accessed 20 January 2022).
- Peli, T. & Malah, D. A study of edge detection algorithms. *Comput. Graph. Image Process.* **20**, 1–21 (1982).
- Mori, N., Suzuki, T. & Kakuno, S. Noise of acoustic Doppler velocimeter data in bubbly flows. *J. Eng. Mech.* **133**, 122–125 (2007).
- Torrence, C. & Compo, P. A practical guide to wavelet analysis. *Bull. Am. Meteorol. Soc.* **79**, 61–78 (1998).
- Meteorological Stations, NOAA Tides and Currents (National Oceanic and Atmospheric Administration, accessed 20 January 2022).
- Ocean Data Buoy Observations (Japan Meteorological Agency, accessed 20 January 2022).
- Fiji Meteorological Service, Climate Services Division/Department of Meteorology, Ministry of Infrastructure, Transport, Disaster Management & Meteorological Services (accessed via data request).
- Duncombe, J. The surprising reach of Tonga's giant atmospheric waves. *Eos* <https://doi.org/10.1029/2022EO220050> (2022).
- Amazon Web Services Portal for GOES 17 Data <https://noaa-goes17.s3.amazonaws.com> (accessed 7 April 2022).
- Wei, G., Kirby, J. T., Grilli, S. T. & Subramanya, R. A fully nonlinear Boussinesq model for surface waves. Part 1. Highly nonlinear unsteady waves. *J. Fluid Mech.* **294**, 71–92 (1995).
- Vilibić, I., Monserrat, S., Rabinovich, A. & Mihanović, H. Numerical modelling of the destructive meteotsunami of 15 June, 2006 on the coast of the Balearic Islands. *Pure Appl. Geophys.* **165**, 2169–2195 (2008).
- Regional: Pacific Disaster Resilience Program, Multi-Hazard Risk Assessment, Tongatapu Technical Risk Assessment, Report prepared by Arup Australia for Asian Development Bank Project 50028-001 (ADB, 2021).
- Borrero, J., Greer, D., McIntosh, R. & Damlamian, H. Tsunami hazard assessment for Tongatapu, Tonga. In *Proc. Australasian Coasts & Ports 2021 Conference* (2021).
- Le Méhauté, B. & Wang, S. *Water Waves Generated by Underwater Explosion* Vol. 10 (World Scientific, 1966).
- Dragoni, M. & Santoro, D. A model for the atmospheric shock wave produced by a strong volcanic explosion. *Geophys. J. Int.* **222**, 735–742 (2020).
- Lynett, P. J., Wu, T. R. & Liu, P. L. F. Modeling wave runup with depth-integrated equations. *Coast. Eng.* **46**, 89–107 (2002).
- Sitanggang, K. I. & Lynett, P. Parallel computation of a highly nonlinear Boussinesq equation model through domain decomposition. *Int. J. Numer. Methods Fluids* **49**, 57–74 (2005).

Publisher's note Springer Nature remains neutral with regard to jurisdictional claims in published maps and institutional affiliations.

Springer Nature or its licensor holds exclusive rights to this article under a publishing agreement with the author(s) or other rightsholder(s); author self-archiving of the accepted manuscript version of this article is solely governed by the terms of such publishing agreement and applicable law.

© The Author(s), under exclusive licence to Springer Nature Limited 2022

Water level time series processing and spectral analyses

The New Zealand tide gauge data were obtained from the GeoNet programme of New Zealand's Institute of Geological and Nuclear Science. The GeoNet stations are referred to by a four-letter code, such as AUCT for Auckland. We downloaded the 1 Hz LTT dataset, which is provided with the tide signal removed from a publicly accessible file transfer protocol (FTP) server. We then processed the 1 Hz data by despiking using the *rmoutliers* function in Matlab, which removed any outliers more than four standard deviations from the mean of a 100-element moving window. A high-pass filter was applied with a cut-off of 250 min to remove any residual tidal components.

Deep-water tsunami data were obtained from NOAA's array of DART tsunameters deployed throughout the Pacific Ocean, and from the New Zealand DART array. When in normal operation, DART gauges sample every 15 min but when they are triggered, on detection of an event, the sampling rate is increased to 15 s. Only 15 s data were used in this analysis. Spikes were identified using the *rmoutliers* routine⁴⁴ and subsequently removed by manual inspection. A subsequent high-pass filter was applied with a cut-off of 250 min to remove any residual tidal components. For both tide station and DART data, application of the outlier threshold, and low- and high-pass cut-off periods, yielded a clean signal with a consistent division between tide and tsunami periods.

Continuous wavelet transform (CWT) follows the evolution of the frequency content of sea level records over the duration of tsunami events. It performs a similar function to that of short-term Fourier transform in that it can be used to analyse time series containing non-stationary power at many different frequencies, as is the case here where dominant observed frequencies are dependent on the interaction between the incoming tsunami and resonant frequencies of the receiving environment. CWTs were undertaken using the Matlab *cwt* routine using a Morlet wavelet, because it is complex and therefore useful for identification of changes in frequency components over time. It is also a wavelet that has moderate width in both the time and frequency domain, allowing for reasonable resolution in both dimensions⁴⁵. The results of this analysis produce highly redundant, but informative, spectrograms of sea level time series.

Example time series plots of GeoNet and DART data are shown in Extended Data Fig. 1 for Wellington harbour tide station and the NZG DART sensor. The Wellington harbour data are an excellent example of the persistence of this event, with tsunami impacts observed in the harbour for more than 30 h after the arrival of the initial waves. The CWT also shows energy banding in the resonance modes of the harbour at periods of 25 and 160 min. The NZG DART is the closest deep-water sensor to the source. From the CWT, the arrival of the leading waves, with periods of 10–40 min, is followed by a packet of much shorter wave energy, with periods of less than 5 min.

Pressure time series processing

The 134 unique pressure time series were sourced from the following authorities. All pressures from the United States were collected from NOAA's National Data Buoy Center and were sampled at 6 min⁴⁶. Data from Japan were collected from the Japan Meteorological Agency and had 10 min sampling⁴⁷. Fiji pressure data were collected from the Fiji Meteorological Service and were sampled at 10 min⁴⁸. Tonga data were collected from the Nomuka and Nuku'alofa all-weather stations and were sampled every 10 min. All pressure time series were collected starting on 15 January at 00:00 UTC until 16 January at 23:59 UTC.

Distances from the explosion were calculated as Euclidean 'as the crow flies' distance (in kilometres) from the weather station to the location of Hunga Tonga island (−20.536000, −175.382000) using the Haversine equation implemented in Python, which assumes a spherical Earth and ignores ellipsoid effects. Distances were calculated in kilometres, rounded to the nearest 0.1 m.

Pressure was first normalized to the first pressure reading of the time series, to capture change in pressure in contrast to background pressure, thereby standardizing comparisons across pressure gauges. Each time series was high-pass filtered utilizing the MATLAB built-in *highpass* function with a steepness coefficient of 0.99, defining the transition width of the filter as 0.01-fold stopband frequency. For all time series the stopband frequency was set at $1/2 \times 10^4$ Hz, or approximately $1/5 \text{ h}^{-1}$. The filtered signal demonstrated the pressure pulse uncoupled with standard fluctuations in atmospheric pressure at each gauge. Subsequently, the pressure time series was interpolated onto a 10 s time grid over the 48 h sampling period using a cubic spline interpolation, with the time of explosion (04:15 UTC) as the reference time.

The leading pressure pulse was determined by creating a user-defined search window ± 1 h from the estimated time of arrival. For example, the Fiji pressure data search window was between 1 and 3 h post-eruption because the pressure pulses in Fiji arrived approximately 2 h after the eruption. Once the leading pressure pulse was established, the MATLAB built-in minimum and maximum functions were applied to determine the amplitude of the leading pressure pulse and subsequent trough, as well as the corresponding time of arrival for each value and pulse duration. The duration of the positive leading pulse is defined as the time between pressure readings of 20% of the maximum pressure of the pulse; for example, if the pulse has a peak pressure of 1 hPa, the duration would be calculated as the time from when the pulse amplitude increases by more than 0.2 hPa to when it decreases by less than 0.2 hPa. For each time series, the following values were recorded: (1) pulse and trough amplitude normalized to individual pressure gauge, (2) pulse and trough arrival time in seconds since the explosion and (3) pulse duration in seconds.

GOES-17 satellite image processing

As recorded immediately after the eruption⁴⁹, the pressure pulse was detected in GOES-17 imagery. The GOES-17 satellite provides infrared imagery covering the Pacific Ocean at intervals of 10 min. Here we use the baseline imagery in Band 13 (10.18–10.48 μm , Clean IR Longwave Window) from 15 January 04:00–16:00 UTC. Data are retrieved from the Amazon Web Services GOES-17 portal⁵⁰. Note that all data created and scripts used to perform this analysis can be found in the open data repository associated with this paper.

To extract the pressure pulse signal from GOES imagery, each image is first converted from the given image coordinates into geographic coordinates. Next, for each pixel in the image, a distance (in kilometres) and azimuth angle from the volcano source are calculated using the techniques described in the previous section. The image data are transformed into a two-column dataset, with one column the radial distance from the source and the second the image intensity. The data are sorted by distance, and window-averaged over a 5 km window.

From inspection of the imagery it is evident that the pressure pulse signal has a relatively commonplace signature in space, in terms of length scale and intensity, but an uncommon signature in time due because of its rapid speed. Thus, to extract the pressure signal we subtract a 'background' intensity from the radial-distance-sorted data, in which the background intensity is defined as the average intensity at each pixel over a 50 min window centred at the current analysis time—for example, when trying to extract the pulse at a time of 05:10 UTC the images at 04:50, 05:00, 05:10, 05:20 and 05:30 UTC are averaged to create the background intensity. Subtracting the background is conceptually similar to taking a time derivative of the image intensity at each image pixel location. Therefore it must be noted that, because the crest and trough of the pulse are each in the order of 20 min in duration, 10 min sampling will result in significant aliasing artefacts in this background-subtraction operation, particularly within the first 1,500 km from the source where the crest and trough amplitude are changing rapidly over time.

The final step in GOES-17 image processing is application of a low-pass filter, with a wavelength cut-off of 300 km, on the radial-sorted and

background-subtracted image intensity data. The result is a clean pressure pulse signature with signal-to-noise ratio of more than 5 up to 9,000 km from the source. Extended Data Fig. 2 provides a time-stack of GOES-17-derived pressure pulse. Using a zero-crossing threshold, the front and rear locations of the crest of the pressure pulse at 10 min intervals can be readily determined and the mean crest location, found using an image-intensity-weighted location, can be calculated. Dividing the mean crest location by the time since generation of the pulse yields the time-averaged crest speed, whereas differentiating the crest location with respect to time gives the local, instantaneous pulse speed, which is not dependent on generation time. The instantaneous crest speed is calculated to be $311 \pm 20 \text{ m s}^{-1}$ over the distance range of 2,000–9,000 km from the source, with the value following \pm being the standard deviation of the dataset (standard deviation represents the scatter in celerity over this distance). Using a generation time of 04:15 UTC, the time-averaged crest speed at a distance of 9,000 km is 306 m s^{-1} (note that, at this distance, speed is controlled by the pulse propagation data to the east and north because the imagery does not cover this distance to the south and west).

We repeat this analysis with azimuthally partitioned data. We divide the imagery data into four bins each covering 90° of angle from the source, with one bin centred on each of the compass directions of east, south, west and north. This analysis allows us to quantify potential differences in speed as a function of the direction of travel away from the source. We find the following time-averaged crest speeds (with a generation time of 04:15 UTC):

- east bin (compass angles $45\text{--}135^\circ$): 307 m s^{-1} at a distance of 8,000 km
- south bin (compass angles $135\text{--}225^\circ$): 317 m s^{-1} at a distance of 8,000 km
- west bin (compass angles $225\text{--}315^\circ$): 309 m s^{-1} at a distance of 5,500 km
- north bin (compass angles $315\text{--}45^\circ$): 306 m s^{-1} at a distance of 8,000 km

and instantaneous crest speeds (celerity):

- east bin (compass angles $45\text{--}135^\circ$): $313 \pm 22 \text{ m s}^{-1}$
- south bin (compass angles $135\text{--}225^\circ$): $327 \pm 48 \text{ m s}^{-1}$
- west bin (compass angles $225\text{--}315^\circ$): $317 \pm 27 \text{ m s}^{-1}$
- north bin (compass angles $315\text{--}45^\circ$): $312 \pm 25 \text{ m s}^{-1}$

where instantaneous crest speeds in the east, south and north bins are calculated over the distance range 2,000–8,000 km, and in the west bin at 2,000–5,500 km from the source. There is a statistically significant directional dependence on the speed of the pressure pulse, suggesting that different pulse speeds would be found with different regional datasets. Finally we note, from inspection of Extended Data Fig. 2, that additional wave modes (gravity and other acoustic modes) are present at early times and close distances to the source.

Air-pressure pulse model

To capture the propagation of the air-pressure pulse across the Pacific Ocean we developed an empirical pressure pulse evolution model. The general form of the air-pressure N-wave model is:

$$P(r, t) = p_{\text{crest}} \times e^{-\theta_{\text{crest}}} - p_{\text{trough}} \times e^{-\theta_{\text{trough}}}$$

where P is the time and space-varying function of air pressure (Pa), r is the distance from the volcano source (m), t is the time post eruption (s), p_{crest} and p_{trough} are the time-dependent amplitude of the leading pressure crest and trailing pressure trough, respectively (Pa) and θ_{crest} and θ_{trough} are the square of the time- and space-dependent phase function of the pressure crest and pressure trough, respectively.

To determine the empirical relationship for crest and trough amplitude, we performed a statistical analysis on the 134 weather station pressure observations throughout the globe. For each observation we determined crest amplitude, trough amplitude, crest arrival time and trough arrival time. Through minimization of error between observation and empirical fit, we find the following relations:

$$c_{\text{crest}} = 306 \times \tanh\left[\frac{t + 300}{4,000}\right]$$

$$c_{\text{trough}} = 295 \times \tanh\left[\frac{t}{7,000}\right]$$

$$p_{\text{crest}} = \frac{2.2 \times 10^6}{2\pi R_c^{0.5}} \times \tanh\left[\frac{R_c}{3.0 \times 10^5}\right]^2$$

$$p_{\text{trough}} = \frac{8.0 \times 10^8}{2\pi(R_t + 2.0 \times 10^5)^{0.9}}$$

where c_{crest} is the time-averaged wave speed of the crest at time t (m s^{-1}), c_{trough} is the time-averaged wave speed of the trough at time t (m s^{-1}), $R_c = c_{\text{crest}} \times t$ is the radial distance the crest has travelled at time t (m) and $R_t = c_{\text{trough}} \times t$ is the radial distance the trough has travelled at time t (m).

These trends, as well as the observed data, are shown in Extended Data Fig. 3. Note that with the assumption of a pressure pulse generation time of 04:15 UTC, to match the observed arrival time of the pressure crest in the near field the time-averaged crest speed must be increasing in time in the near field. There is no generation time that yields a constant pulse celerity in the near field, as dictated by the Tonga and Fiji observation data. For example, the Tongatapu (68 km from the volcano) pressure pulse crest arrives at 04:25 UTC whereas in Ono-i-Lau, Fiji (350 km from the volcano) and Nadarivatu, Fiji (760 km from the volcano) the pressure crest arrives at 04:48 and 05:15 UTC, respectively. Then, assuming that the pressure pulse is generated at the volcano and using a constant celerity of 311 m s^{-1} , the Tongatapu data would suggest a generation time of 04:21 UTC whereas the Fiji data would imply a generation time of 04:29 UTC from the Ono-i-Lau data and 04:34 UTC from the Nadarivatu data. Because the pulse crest cannot be generated later than 04:25 UTC (because it was observed at this time), the celerity of the pressure pulse in the immediate near field must be increasing in time. Assuming radial symmetry, the average speed of the pulse crest between the Tongatapu and Ono-i-Lau radial distances is 204 m s^{-1} whereas that between Ono-i-Lau and Nadarivatu is 253 m s^{-1} . The apparent pressure pulse celerity variation in the near field, as implied by the surface pressure data, may be due to both transient-generation effects and the superposition of different modes and frequencies. Finally, we remark that the crest pressure expression includes the tanh function, which acts to reduce the amplitude of the positive-pressure pulse near to the source. This is a required modification and is indicated by the pressure data measured in Tonga and Fiji.

With these data-fitted trends, the square of the phase function is given as $\theta_{\text{crest}} = \left(\frac{r - R_c}{0.75 \times L_c}\right)^2$ and $\theta_{\text{trough}} = \left(\frac{r - R_t}{0.75 \times L_t}\right)^2$, where L_c and L_t are the time-dependent length scales of the crest and trough, respectively. These length scales are calculated as the product of the speed and period of the crest and trough. Here, we attempted to determine the period of these pulses using a statistical analysis of the time series but found that the scatter in these observed periods was extremely large, due mainly to the transient nature of the pressure pulse and noise in the pressure observations at similar periods to the pulse. Thus, we use the data trends as a guidance but tune the period calculations based on an error minimization between the predicted pressure time series and observed pressure time series at the 134 locations. Using this procedure, we find that

$$T_{\text{crest}} = 2,300 \times t^{-0.1}$$

$$T_{\text{trough}} = 3,300 \times t^{-0.1}$$

where both terms have units of seconds. With this pressure pulse model we can recreate the average behaviour of the pulse throughout the Pacific, away from the immediate near field. Various model–data comparisons are given in Extended Data Fig. 4. The pressure waveform is accurately captured by the model, including at the near-field stations. We note that the purpose of this model is to recreate the observed pressure time series, in arrival time, period and amplitude; regardless of the generation time used, this matching of pressure records ensures that the tsunami model is forced with the observed pressure. As evident from the New Zealand observations, topography and local weather can play a second-order role in modifying the shape and arrival time of the waveform. In the far field, including stations in Japan and the United States, although model data agreement is still high the pressure pulse signal begins to approach the natural noise, or local pressure fluctuations. Therefore, clear identification of air-pressure pulse becomes increasingly difficult.

Boussinesq water wave model

Tsunami propagation is simulated using Boussinesq-type equations, which are a depth-integrated form of Navier–Stokes equations valid for weakly dispersive and strongly nonlinear waves³⁴. The Boussinesq-type model incurs a substantial computational cost in comparison with the shallow water wave equations traditionally used for tsunami predictions. However, as shown by the high-frequency energy observed in the DART stations in the range 3–5 min, we expect that dispersion may play an important role in this event. In water depths up to 10 km, the extended Boussinesq-type equations solved by COULWAVE should provide excellent linear dispersion accuracy for periods over 2 min (ref. ⁵¹). The air-pressure pulse is coupled with the tsunami through a gradient-forcing term in the momentum equations⁵². Thus, the air-pressure pulse can contribute energy to the ocean but not the reciprocal, because the empirical form of the air-pressure model implicitly includes ocean coupling that occurred during the event.

Simulations are performed on three different nested grids. The first, or local, grid is centred on the volcano and includes the islands in its immediate vicinity. The dimensions of this grid are 170 × 200 km², with a constant grid resolution of 100 m. Simulations in this grid provide the tide station comparison shown in Fig. 4. To account for the arrival of the leading waves of the tsunami at high tide, the seafloor and topography elevations—given relative to mean sea level (MSL)—are shifted downward by 0.45 m, equivalent to the elevation difference between MSL and tide elevation at tsunami arrival.

The second, or South Pacific, grid, includes Fiji and New Zealand, with coverage from latitude 45° S to 0° and longitude 160° W to 180° W. A constant grid resolution of 1 km is used for this domain. Simulations in this grid provide the New Zealand DART comparisons shown in Fig. 4.

The third grid is the Pacific-wide grid, with coverage from latitude 80° S to 80° N and longitude 160° W to 120° E. A constant grid resolution of 3 km is used for this domain. Simulations in this grid provide the US NOAA DART comparisons shown in Fig. 4.

For the local grid, bathymetry and topography are both sourced from a high-resolution dataset that integrates the general bathymetric chart of the oceans (GEBCO), nautical charts, LiDAR topography, multi-beam bathymetry data, other offshore surveys and hand-digitized data. The bathymetry was compiled as part of a multi-hazard assessment project sponsored by the Asian Development Bank^{53,54}. For the South Pacific and Pacific-wide grids, the GEBCO 15-arcsecond (2021) dataset is used. The data from these sources are bilinearly interpolated to fit the numerical grid.

Cavity collapse source

For the cavity collapse source, we use a simple radial Gaussian initial condition of the form

$$A \times e^{-(r/W)^2}$$

where r is the distance from the volcano source (m), A is the initial amplitude of the impulse and W is the characteristic length. The simulations presented in this paper use an amplitude of 100 m and a length of 2 km. These values were primarily chosen on the basis of the agreement with observational data, but are also representative of the length scales of the volcano. We remark that one could perform extensive tuning with a set of Gaussian unit sources or published semi-empirical initial conditions for explosion-generated waves⁵⁵ to achieve better agreement at the Nuku'alofa tide gauge. We choose not to include such an analysis here, because neither the complex application of a simple, idealized source nor the very weakly constrained use of a semi-empirical initial condition is justified by the current, limited inventory of near-field observation data.

Shock wave source

The pressure from the early-time shock wave is modelled using analytical expressions for a spherical pulse with a strong shock approximation⁵⁶. The model provides a temporally and spatially varying pressure shock front, which is included in the hydrodynamic model in the same way as the air-pressure pulse model. The shock wave model calculations are primarily dependent on specification of the energy released by the explosion which, at the time of writing, is uncertain. We assume an energy release of 1.0×10^{16} J, which does create a large (>10 m) tsunami near the source but is secondary to the water-cavity source in the near field and insignificant in the far field.

Model simulations

All simulations approximate bottom friction by a quadratic friction drag law, with a friction coefficient of 0.005 (ref. ⁵⁷). No other dissipation models are used with these simulations. Simulations were run on a large computer cluster⁵⁸. The local grid was run on 400 cores and required 10 h of wall clock computation time. The South Pacific and Pacific-wide grids were run on 1,000 cores, and required 10 and 24 wall clock hours, respectively.

Model comparisons with all Pacific DART stations are shown in Extended Data Fig. 5, with six of these comparisons shown in Fig. 4. The model reasonably captures the arrival time, amplitude and, in the majority of comparisons, the multi-frequency train of waves. Furthermore, we include four additional model comparisons at tide stations in the South Pacific, provided in Extended Data Fig. 6. Because the South Pacific grid uses 1 km grid spacing, coastal amplification effects are missing in the model results. Therefore, we have chosen locations that are reasonably represented in the GEBCO database and exist on relatively simple coastlines. We note that the data sampling frequency at the Niuaotupapu tide gauge is 5 min, and thus this signal is unable to resolve the 3–5-min periods found in the model results. Model data agreement is high in those locations that use a 1-min sampling rate.

Data availability

All of the processed data, scripts used to create the Extended Data figures and examples of raw data processing used in this manuscript can be freely accessed at <https://www.designsafe-ci.org/>, referencing Data Depot project no. PRJ-3474 (<https://doi.org/10.17603/ds2-6hx4-ke44>). Pressure data were provided by NOAA (<https://noaa.gov>), the Japan Meteorological Agency (<https://www.jma.go.jp/jma/indexe.html>), the Fiji Meteorological Service (<https://www.met.gov.fj/>) and the Tonga Meteorological Service (<http://met.gov.to/>). DART sensor data were provided by the New Zealand GeoNet project (<https://www.geonet.org.nz/tsunami/dart>) and the US National Data Buoy Center (<https://www.ndbc.noaa.gov/obs.shtml?lat=13&lon=-173&zoom=2&pgm=tsunami>). Tide station records were provided by the Sea Level Station Monitoring Facility (<https://www.ioc-sealevelmonitoring.org/>).

Code availability

The model source code, simulation control and input files and output processing scripts for the COULWAVE simulations presented in this paper can be freely accessed at <https://www.designsafe-ci.org/>, referencing Data Depot project no. PRJ-3474 (<https://doi.org/10.17603/ds2-6hx4-ke44>).

Acknowledgements The University of Southern California (USC) authors were supported by US NSF grant nos. CMMI-1661052, OCE-1830056 and ICER-1940315. Any opinions, findings and conclusions or recommendations expressed in this material are those of the authors and do not necessarily reflect the views of the National Science Foundation. This article has been peer reviewed and approved for publication consistent with USGS Fundamental Science Practices (<https://pubs.usgs.gov/circ/1367/>). Any use of trade, firm or product names is for descriptive purposes only and does not imply endorsement by the US Government. A. Kumar, from the Fiji Meteorological Service, Climate Services Division, assisted in providing the authors with atmospheric pressure data from Fiji. M. Paea, of the Ha'atafu Beach Resort, provided the photographs shown in Fig. 2c,d. The team acknowledges the USC Center for Advanced Research Computing for the 0.5 million central processing unit hours used for this modelling effort.

Author contributions P.L. was responsible for leading the overall team, developing the N-wave pressure pulse model and performing the numerical solutions. M.M. was responsible for performing the Ventura harbour field survey, organizing the manuscript and processing and curating the pressure time series data. Z.Z. was responsible for performing the Ventura harbour field survey, collecting observational data and creating visualizations with the model output. W.R. participated in the Ventura harbour field survey and collected and processed the DART and tide station data. J. Borrero., D.G., O.F. and C.B. collected reports and observations in the near field, processed New Zealand DART and tide station data and contributed to writing of the manuscript. B.J., S.L.S., A.R., A.S., B.N., J. Bolt. and N.G. completed the tsunami field survey of Santa Cruz harbour and surrounding areas, and processed the collected data. B.J., S.L.S. and A.R. contributed to writing of the manuscript. C.S. participated in delineation of source mechanisms and assisted in writing of the manuscript. B.E. and G.E.C. participated in the Ventura harbour field survey and assisted in writing of the manuscript. All authors discussed the results and commented on the manuscript.

Competing interests The authors declare no competing interests.

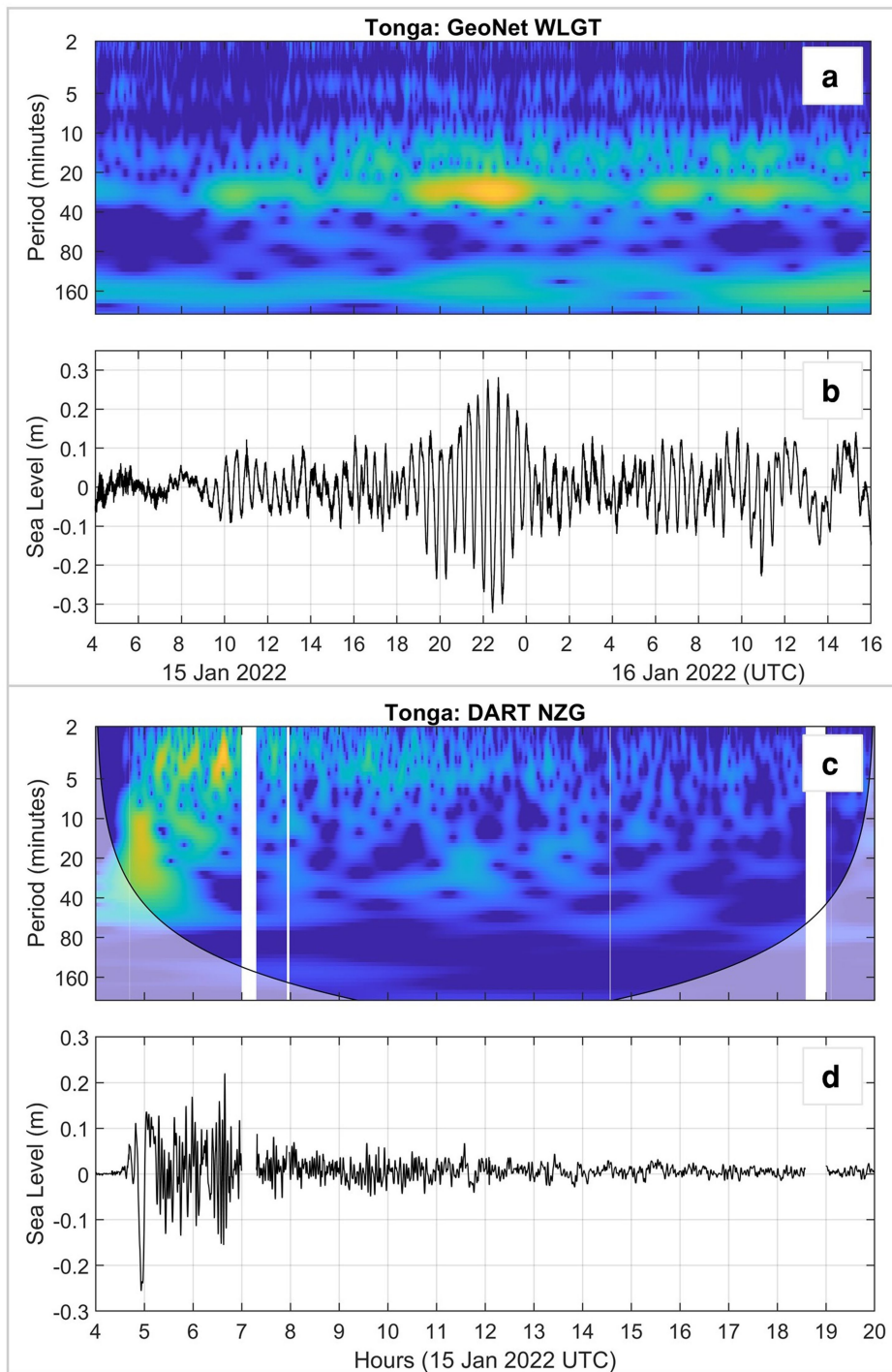
Additional information

Supplementary information The online version contains supplementary material available at <https://doi.org/10.1038/s41586-022-05170-6>.

Correspondence and requests for materials should be addressed to Patrick Lynett.

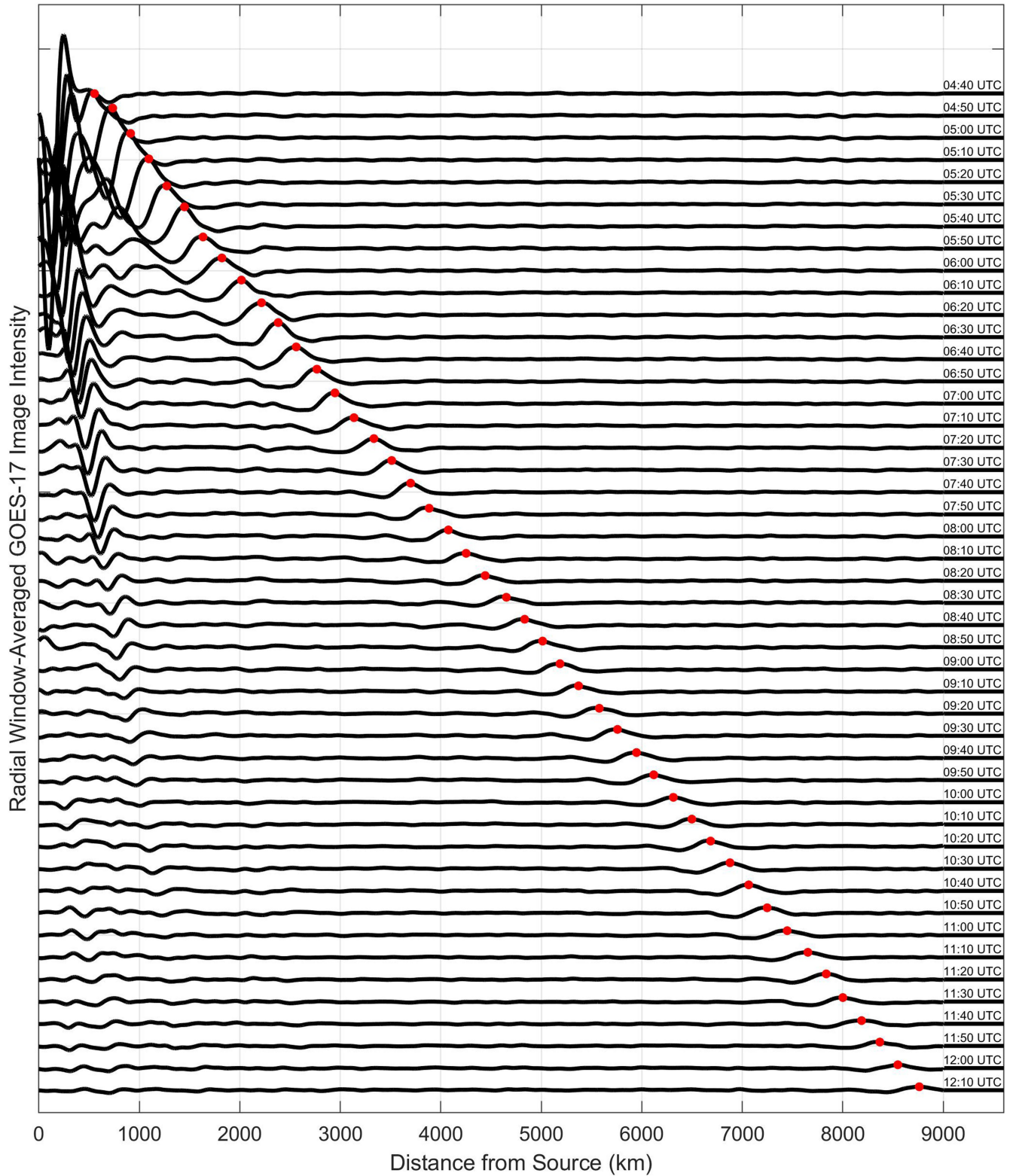
Peer review information *Nature* thanks Stephan Grilli, Raphaël Paris, Colin Whittaker and the other, anonymous, reviewer(s) for their contribution to the peer review of this work.

Reprints and permissions information is available at <http://www.nature.com/reprints>.



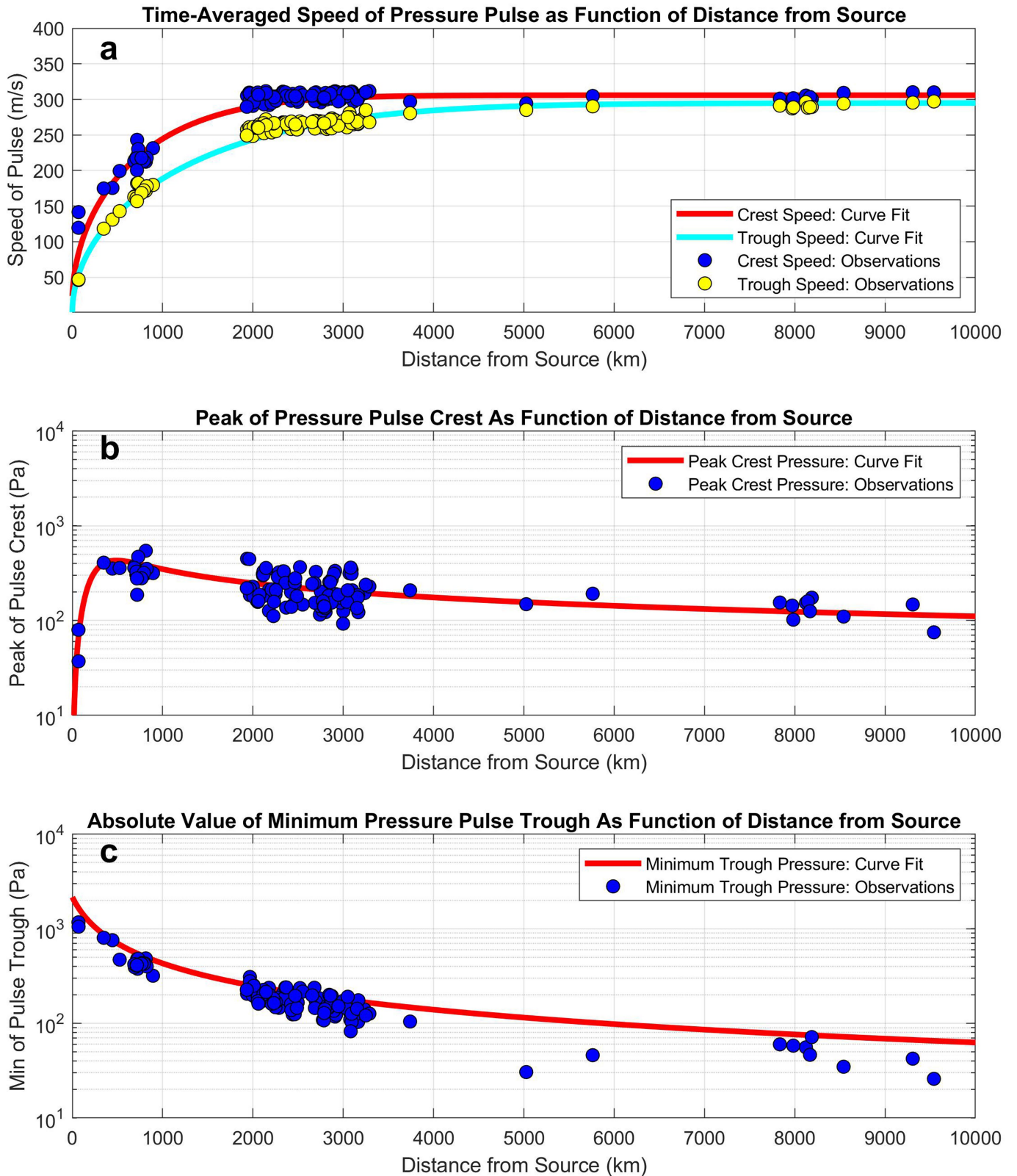
Extended Data Fig. 1 | Example wavelet analysis and filtered time series data. **a, b,** Data for Wellington Harbor, New Zealand showing the (a) wavelet result derived from the (b) observed tide station data obtained from New Zealand’s GeoNet. In the wavelet analysis, note the horizontal banding of energy, indicating the excitation of the resonant modes of the harbor, and the clear increase in energy between 20:00 and 23:00 UTC. **c, d,** Data for DART NZG showing the (c) wavelet result derived from the (d) observed DART sensor data

from GeoNet. The parabolic black lines found on the lower left and right corners of the wavelet plot denote areas of the wavelet surface that may suffer from tapering effects. The white areas identify times of no data from the sensor. The wavelet surface shows the energetic initial arrival of the tsunami with periods of 10–20 min near 05:00 UTC, followed by pulses of energy in the 3–5 min period range.



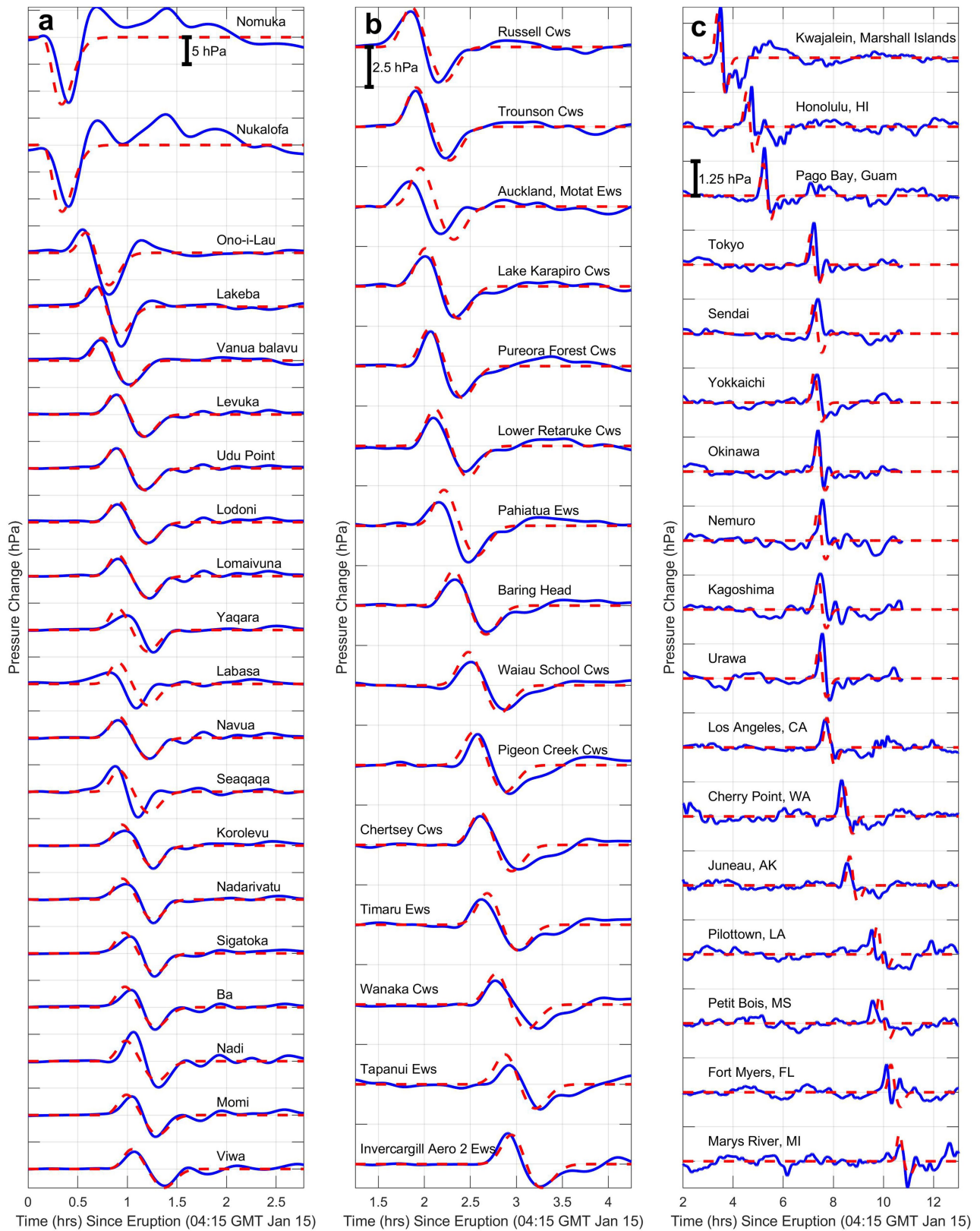
Extended Data Fig. 2 | Time stack of the radially-sorted, window-averaged, and low-pass filtered GOES-17 satellite data. Time series are given at numerous time-stamps on January 15, as given along the right edge of the figure. The peak of the (Lamb wave) pressure pulse crest for each time series is given by the red dots. The distance coordinate of the red dot in each time series

divided by the time since generation yields the time-averaged pulse speed, while the difference in successive pulse crest locations divided by the time between the two images (10 min) gives the instantaneous speed of the pulse, or the celerity. GOES-17 data provided by NOAA.



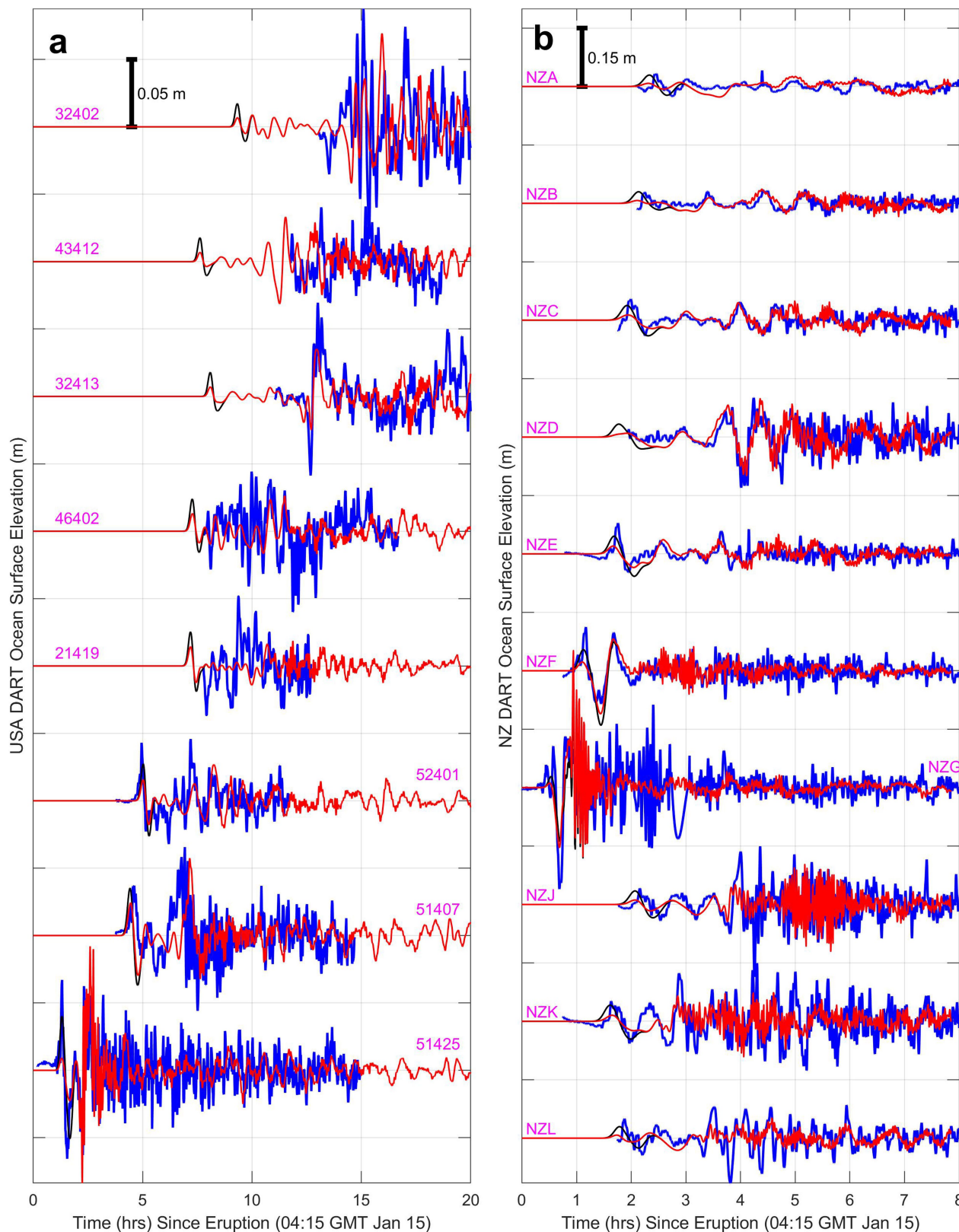
Extended Data Fig. 3 | Bulk calibration curve fits for the N-wave pressure pulse model. a. Data (dots) and curve fit (lines) for time-averaged speed of the crest and trough, assuming a generation time of 04:15 UTC. **b.** Data (dots) and curve fit (lines) for crest amplitude of the pressure pulse. **c.** Data (dots) and

curve fit (lines) for trough amplitude of the pressure pulse. Pressure data provided by NOAA, the Japan Meteorological Agency, the Fiji Meteorological Service, and the Tonga Meteorological Service.



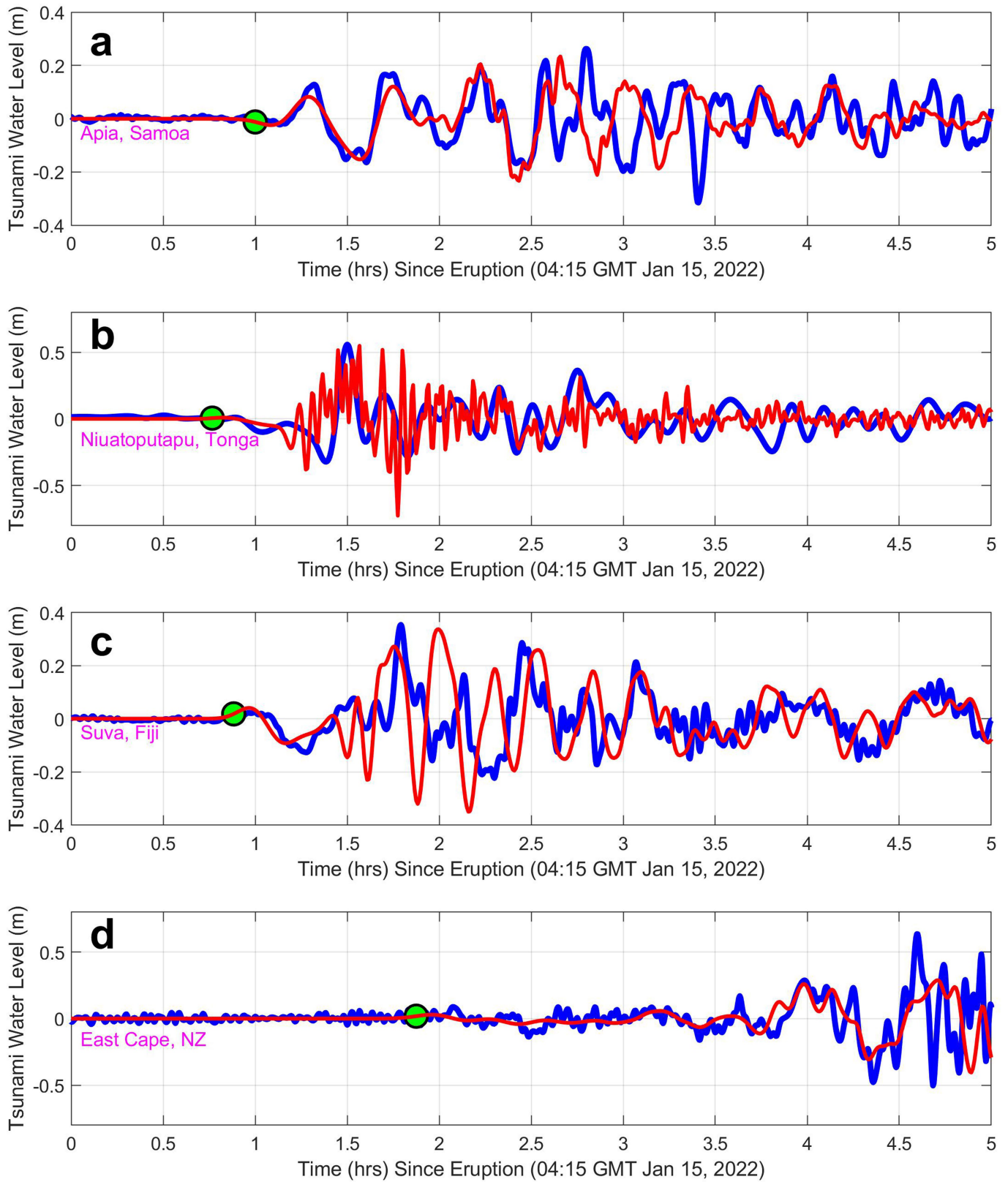
Extended Data Fig. 4 | Summary of modeled pressure time series comparisons with observed data. a, b, c. Filtered observed data (blue lines) and model prediction (red dashed lines), where comparison location is given by the text, for (a) data stations in Tonga and Fiji, (b) data stations in New Zealand,

and (c) various locations in the far-field. Note that the vertical pressure scale is given in the upper part of each column. Pressure data provided by NOAA, the Japan Meteorological Agency, the Fiji Meteorological Service, and the Tonga Meteorological Service.



Extended Data Fig. 5 | DART sensor ocean-surface-elevation time series comparisons. a, b, Filtered DART data (blue lines), model predictions (red line), and model predictions with pressure head from pressure pulse added (black line), where sensor name is given by the text, for (a) DART stations in the

USA network, and (b) DART stations in the New Zealand network. The geographic location of these sensors is provided in Figure 3. Note that the vertical ocean surface elevation scale is given in the upper part of each column. DART data provided by NOAA and New Zealand's GeoNet.



Extended Data Fig. 6 | Tide station ocean-surface-elevation time series comparisons. a, b, c, d, Filtered tide station data (blue lines) and model prediction (red lines) for (a) Apia, Samoa, (b) Niuatoputapu, Tonga, (c) Suva, Fiji, and (d) East Cape, New Zealand. The green circle denotes the arrival time of the crest of the pressure pulse. Tide station data retrieved from the Sea Level Monitoring Facility.

Fiji, and (d) East Cape, New Zealand. The green circle denotes the arrival time of the crest of the pressure pulse. Tide station data retrieved from the Sea Level Monitoring Facility.